

Numerical Estimation of the Geometry and Temperature of An Alternating Current Steelmaking Electric Arc

Jesús D. Hernández,* Luca Onofri, and Sebastian Engell*

A channel arc model (CAM) that predicts the temperature and the geometry of an electric arc from its voltage and impedance set-points is presented. The core of the model is a nonlinear programming (NLP) formulation that minimizes the entropy production of a plasma column, the physical and electrical properties of which satisfy the Elenbaas–Heller equation and Ohm's law. The radiative properties of the plasma are approximated utilizing the net emission coefficient (NEC), and the NLP is solved using a global numerical solver. The effects of the voltage and impedance set-points on the length of the electric arc are studied, and a linear formula that estimates the length of the arc in terms of its electrical set-points is deduced. The length of various electric arcs is measured in a fully operative electric arc furnace (EAF), and the results are used to validate the proposed models. The errors in the predictions of the models are 0.5 and 0.4 cm. In comparison, the existing empirical and Bowman formulae estimate the length of the experimental arcs with errors of 2.1 and 2.6 cm. A simplified formula to estimate the temperature of an electric arc in terms of its electrical set-points is also presented.

of voltage and impedance for the electric arc. During the process, the control system of the electrodes manipulates the length of the electric arc—by moving the electrodes up and down—in such a way that predetermined set-points are achieved. In the industry, it is known that the length of the arc can be manipulated by changing the voltage or impedance of the arc. On the other hand, the influence of these two variables on the temperature of the arc has not yet been addressed in detail in the literature. Understanding the effects of the electrical set-points on the physical properties of the arc is fundamental to any optimization of the process because the heat exchange mechanisms from the arc to the metal mostly depend on the power, the temperature, and the geometry of the electric arc.

Traditionally, the behavior of alternating current (AC) steelmaking arcs has been studied using models that couple the electrical model of the high-voltage circuit of the

1. Introduction

Two of the most important operative parameters of the steel production process via electric arc furnaces (EAFs) are the set-points


EAF with a) complex magnetohydrodynamic (MHD) models^[1,2] or b) simplified direct current channel arc models (DC-CAMs).^[3] The main advantage of the latter group of models is that they can provide satisfactory approximations to the most relevant properties of the arc at very low computational costs and therefore, they can be integrated in more elaborated EAF models for online simulations or optimization purposes.

Existing AC-CAMs rely on the assumption that at each point in time an AC arc can be approximated by the steady state of a DC counterpart carrying the same electrical current.^[4–6] In these models, the external AC circuit is used to compute the electrical current and then, at each instant in time, all the properties of the DC plasma column are computed. Arguably, two of the weakest points of these models are that, on the one hand, they require an a priori knowledge of the length of the arc to compute the radius and the radiation losses of the arc. On the other hand, they assume a constant arc temperature that is independent on the electrical set-points.^[7] This assumption is problematic because it decouples the radiative and conductive properties of the plasma column from the very phenomena that govern them: the current and the voltage of the arc.

In this work, concepts of plasma physics are utilized to develop a model that can predict the effect of the electrical set-points on the geometry, the temperature, and the conductive and radiative properties of the AC electric arc. Our goal is to derive an accurate model of the electric arc in steelmaking that is appropriate for process simulation and optimization.

J. D. Hernández, Prof. S. Engell
Process Dynamics and Operations Group
Department of Biochemical and Chemical Engineering
Technische Universität Dortmund University
Emil-Figge-Straße 70, Dortmund 44227, Germany
E-mail: jesus.hernandez@tu-dortmund.de;
sebastian.engell@tu-dortmund.de

Dr. L. Onofri
Process Control and Automation Department
Acciai Speciali Terni
Vle. B.to. Brin 218, Terni 05100, Italy

 The ORCID identification number(s) for the author(s) of this article can be found under <https://doi.org/10.1002/srin.202000386>.

© 2020 The Authors. Steel Research International published by Wiley-VCH GmbH. This is an open access article under the terms of the Creative Commons Attribution License, which permits use, distribution and reproduction in any medium, provided the original work is properly cited.

The copyright line for this article was changed on 12 December 2020 after original online publication.

Correction added on 16 December 2020, after first online publication: Projekt Deal funding statement has been added.

DOI: 10.1002/srin.202000386

The rest of this article is structured as follows. Section 2 introduces the theoretical foundations needed to build the arc model, which is later derived in Section 3. Section 4 presents the experimental procedures and the results of the measurements of the length of various electric arcs in a fully operative EAF. Section 5 is devoted to present and discuss the results of the numerical simulations, and simplified formulas to estimate the length and the temperature of the electric arc from its electrical set-point are derived. In Section 6, the errors in the predictions of the models presented here are quantified and their performance is compared with that of state-of-the-art arc models. This manuscript is wrapped up in Section 7 with conclusions and final remarks.

2. Theoretical Background

Since the 1950s, the behavior of DC arcs has been studied using the plasma steady-state energy equation, known as the Elenbaas–Heller equation.^[8] Historically, this equation has been solved for low-power arcs with no radiation losses by making approximations of the nonlinear plasma properties.^[9] Later in the early 1970s, Lowke classified electrical discharges according to their electrical and radiative properties, and the characteristics of radiation-dominated arcs were stated.^[10,11] In these studies, the relationships between the electrical field and the current, as well as between the temperature and the radius for electric arcs with currents of up to 2000 A at a pressure of 30 atm, were studied. At around the same time, the properties of steelmaking arcs were also analyzed experimentally, and approximations of the velocities, geometries, and temperatures of the arc, at voltages from 70 to 140 V and currents from 4 to 8 kA, were provided.^[12,13] More recently, scientists have used iterative methods to calculate the temperatures profiles of electric arcs by solving Ohm’s law and the full radiative Elenbaas–Heller equation for arcs of predetermined geometries and wall temperatures.^[14] In all the previous cases, finding a solution to the problem was possible because the geometry of the electric arc was known: the length of the arc was the distance between the electrodes (fixed) and the radius of the arc was measured from experimental observations.

On the other hand, obtaining a solution of the integrated system of Ohm’s law and the Elenbaas–Heller equation is not possible for steelmaking arcs because for a given voltage and impedance set-point, the geometry of the arc is not known. Thus, the system of equations is underspecified (two equations, three calculated variables). In many studies, the Steenbeck’s minimum energy principle (minimum voltage) was used to obtain an additional equation to obtain a unique solution.^[15,16] Although a theoretical derivation from first principles is still outstanding, this approximation has for long been accepted as it reproduces experimental observations well.^[17] Traditionally, Steenbeck’s principle has been associated with the principles of minimum and maximum entropy production (MinEPP, MaxEPP). Using either the MinEPP or the MaxEPP to obtain an additional equation requires a careful consideration because as it is recognized in the literature, the use of one or another is contradictory and to a certain extent, case dependent.^[18,19]

In his work, Di Vita^[18] argues that “depending on the problem, equilibrium is described either through maximization or minimization of some macroscopic quantity” and that “no

universal criterion of stability for steady states of systems with dissipation exist but the second principle of thermodynamics.” Ten cases, each with a given quantity to be minimized or maximized, and a set of constraints to be satisfied are postulated.

This work utilizes the most general case of those exposed by Di Vita^[18] to demonstrate that the geometry and temperature of a steelmaking arc can be calculated using the MinEPP and uses nonlinear programming (NLP) to solve the minimization problem of the entropy production of the arc. The problem is constrained to Ohm’s law, the Elenbaas–Heller equation, and the conductive and radiative properties of the plasma. Boundaries of the temperature domain were set to ensure that the assumption of a thin isothermal radiation-dominated plasma holds, and the boundaries of the arc length domain were chosen to satisfy the operative practices of the steelmaking process. Finally, the bounds for the radius are selected based on experimental data.

3. The Electric Arc Model

3.1. Assumptions

The following set of assumptions are made.

1) Geometrical: The arc can be modeled as a wall stabilized plasma column due to the stabilizing effect of the flow of air created by Meacker’s effect.^[20] The instabilities created by the inversion of the arc polarity during an AC cycle are neglected; 2) Physical: A uniform constant pressure in the plasma and a weak convection both inside and outside of the plasma are assumed. Therefore, the effect of the external flow on the external heat loss is negligible. The energy spent on accelerating the air flow at the external cathode end of the plasma (Maecker’s effect) is neglected as it is many orders of magnitude smaller than the losses by radiation. The same applies to any Lorentz force in the plasma; 3) Electrical: The electrical current flows perpendicular to the cross section of the arc and is uniformly distributed. The electric field only has an axial component which is independent of the radius. Magnetization due to internal and external current flows is neglected; 4) Other: Local thermodynamic equilibrium (LTE) and a thin plasma condition.

3.2. The AC Arc as a Static Inductive Load

In the phasor domain, the electric AC arc is commonly modeled as an inductive impedance (Z_a) composed of a resistor (R_a) and an inductance (L_a) connected in series.^[20] The static root mean squared (RMS) quantities for the voltage, the current, and the real power of the AC arc can be computed in terms of the original AC quantities, as in Equation (1)–(4).

$$R_a = Z_a \cos\phi \quad (1)$$

$$V_{a,R} = V_a \cos\phi \quad (2)$$

$$I_a = \frac{V_a}{Z_a} \quad (3)$$

$$P_a = \frac{V_a^2}{Z_a} \cos\phi \quad (4)$$

Above, V_a and Z_a are the AC voltage and impedance set-point of the electric arc. $\cos\phi$ is the measured power factor of the arc, which in normal operations varies between 0.76 and 0.90.

3.3. Governing Equations

The physical and electrical phenomena of a wall stabilized DC plasma column in LTE with negligible Lorentz forces are governed by the Elenbaas–Heller energy Equation (5) and Ohm’s law (Equation (6)).^[8,14,21]

$$\nabla \cdot (-\kappa \nabla T) + \nabla \cdot \vec{q}_{\text{rad}} = \vec{j} \cdot \vec{E} \quad (5)$$

$$\vec{j} = \sigma(T) \cdot \vec{E} \quad (6)$$

Equation (5) contains from left to right a conductive term, a radiation term, and the Joule heating term. Here, \vec{q}_{rad} , \vec{j} , and \vec{E} represent the volumetric radiative flux, the current density, and the electric field. In Equation (6), $\sigma(T)$ is the electrical conductivity of the plasma.

In his works, Lowke^[10,11] proved that optically thin plasmas are radiation dominated and can be considered as isothermal. For this type of arc, the radiative term in Equation (5) can be approximated by means of the net emission coefficient (NEC), as

$$\nabla \cdot \vec{q}_{\text{rad}} = 4\pi \epsilon_N(T, r) \quad (7)$$

The NEC parameter $\epsilon_N(T, r)$ is an experimentally measured quantity that determines the amount of radiation energy that escapes from a cylindrical plasma volume of radius r at temperature T . A plasma is said to be optically thin if its γ parameter, defined as the ratio between $\epsilon_N(T, r)$ and $\sigma(T)$, increases with temperature.

$$\gamma = \frac{\epsilon_N(T, r)}{\sigma(T)} \quad (8)$$

Lowke’s considerations for thin plasmas allow to reduce Equation (5) and (6) to

$$jE = 4\pi \epsilon_N(T, r) \quad (9)$$

$$j = \sigma(T) E \quad (10)$$

The volumetric current density (j) is defined as the infinitesimal flow of charge (I) perpendicular to the cross section of the infinitesimal volume that it traverses (a_{\perp}), and the electric field (E) is estimated as the negative gradient of the electric potential (V).^[22]

$$j = \frac{dI}{da_{\perp}} \quad (11)$$

$$dV = -E dl \quad (12)$$

Integrating Equations (11) and (12) over the cylindrical volume of the arc and replacing these results in Equation (9), the energy equation reads

$$VI = 4\pi^2 \epsilon_N(T_a, r_a) r_a^2 l_a \quad (13)$$

In AC, the complex power of the inductive arc load is composed of an active and the reactive component. The first is the

power consumed by the resistive component of the arc, and the latter is the power that is stored in the magnetic fields of the arc. Considering that only the active power can be transformed from electrical to nonelectrical power,^[23] one can assume that the DC equation can be used to study the effect of the real component of the AC current in the physics of the plasma column. In terms of the resistive component of the AC arc, it follows from Equation (13) that

$$V_{a,R} I_{a,R} = 4\pi^2 \epsilon_N(T_a, r_a) r_a^2 l_a = \frac{V_a^2}{Z_a} \cos\phi \quad (14)$$

In a similar fashion, Equation (10) (Ohm’s law) can be rewritten in terms of the quantities of the resistive component of the AC arc because in the serial inductive branch, the current flowing through the arc and its resistive component is the same. Integrating Equations (11) and (12) and replacing in Equation (10), one obtains

$$\frac{V_{a,R}}{I_{a,R}} = \frac{l_a}{\pi r_a^2 \sigma(T_a)} = Z_a \cos\phi \quad (15)$$

Equation (14) and (15) constitute the main set of equations that describe the behavior of an AC electric arc. There are two specified variables (Z_a and V_a) and three unknown variables (T_a , r_a , and l_a).

According to the most general of the cases discussed by Di Vita,^[18] the steady state of a dissipative medium occurs at the state where $\int dv T^{-1} P_h$ is minimum and the quantities V (voltage) and $\int dv P_h$ are both constant. Here, dv represents the differential volume element and P_h is the dissipated power per unit of volume. The constraints of this variational equations match the boundary conditions of the steelmaking arcs because the operative set-points (voltage and impedance) implicitly set a constant power level of operation. If the $\epsilon_N(T_a, r_a)$ parameter is used in the objective function of the variational equation, one obtains

$$\int dv T^{-1} P_h = \frac{1}{T_a} \int dv 4\pi \epsilon_N(T_a, r_a) = \frac{V_a^2}{Z_a T_a} \cos\phi \quad (16)$$

The RHS term in Equation (16) is the rate of entropy production (S_{gen}) of a DC electric arc.^[24] Therefore, one can conclude that the steady state of an AC arc occurs at the point where the entropy production of its resistive component is minimized.

3.4. Plasma Parameters: Electrical Conductivity and NECs

Equation (14) and (15) depend on the electrical conductivity $\sigma(T_a)$ and the NEC $\epsilon_N(T_a, r_a)$ parameter of the plasma column. Depending on the plasma composition, the values of these properties can be obtained from the literature or computed using the mixing rule

$$\theta_{\text{mix}} = \sum_{i=1}^n x_i \theta_i \quad (17)$$

In Equation (17), θ_{mix} stands for either $\sigma(T_a)$ or $\epsilon_N(T_a, r_a)$, and x for the molar fraction of the component i in the plasma mixture.^[25]

It has been theorized that an industrial steelmaking arc should be composed mainly of air with minor additions of iron and carbon in similar quantities.^[7] In practice, the precise molar fractions of these components are difficult to estimate. As it was demonstrated in various studies, the radiative and conductive properties of air plasmas change dramatically with the addition of metallic and graphite vapors.^[25–27] Therefore, we use a parameter estimation technique to compute the composition of the plasma using experimental data. This procedure is described in detail in Section 4.

The electrical conductivities of pure iron, carbon, and air plasmas were obtained from Gleizes et al.^[25] and Pousse et al.^[28] For the NEC parameters, Bartlova et al.^[26] and Menart et al.^[27] were consulted. In these sources, $\epsilon_N(T_a, r_a)$ is reported in the form of continuous profiles at specific plasma radii of 0.1, 1, and 10 cm. Considering that the radii of steelmaking arcs vary between 5 and 10 cm,^[20] the NEC of the mixture at both 1 and 10 cm is first estimated using Equation (17), and then an appropriate value of the NEC of the mixture for any radius between 1 and 10 cm is computed using a convex combination of these two values, in terms of the arc radius as in Equation (18) and (19).

$$\alpha = \frac{1}{9} (r_a - 1) \quad (18)$$

$$\epsilon_N(T_a, r_a) = (1 - \alpha) \epsilon_{N_{\text{mix}}}(T_a, 1 \text{ cm}) + \alpha \epsilon_{N_{\text{mix}}}(T_a, 10 \text{ cm}) \quad (19)$$

The computed polynomial approximation of $\sigma(T_a)$ and $\epsilon_N(T_a, r_a)$ is provided in Annex A.

3.5. LTE and Plasma Thickness Conditions

The LTE condition and the thin plasma assumption have to hold true for Lowke's approximations to be valid. On the one hand, a plasma is assumed to be in LTE if a sufficiently large ion density exists. For electric arcs, this condition is satisfied for plasma temperatures larger than 10 000 K.^[29] On the other hand, a plasma is said to be optically thin if its γ parameter (Equation (7)) increases with the temperature ($\frac{d\gamma}{dT} > 0$).^[10] The γ parameter and its

derivative with respect to the temperature, in the range from 10 000 to 19 000 K, for three different plasma mixtures at various arc radii, are shown in Figure 1a,b. The studied plasma compositions are as follows.

1) Rich-iron plasma: P1 (9% C–9% Fe–82% air); 2) Moderate-iron plasma: P2 (9.3% C–6.5% Fe–84.2% air); 3) No-iron plasma: P3 (10% C–90% air).

The results in Figure 1a show that as iron is added to the mixture, the radiative properties of the plasma increase faster than the electrical conductivity of the plasma. For this reason, the γ parameter increases with both the temperature and the iron content in the plasma. Figure 1b shows that for the presented mixtures, the thin plasma assumption holds for the temperature range from 10 000 to 17 500 K, for all plasma radii from 3 to 9 cm. Finally, if one considers that a minimum temperature of 12 000 K is required for Equation (17) to be valid,^[25] one can argue that a reasonable temperature range of operation of the arc at which both the LTE and the thin plasma assumptions are satisfied is

$$12\,000 \leq T_a \leq 17\,500 \text{ K} \quad (20)$$

3.6. The Implicit NLP Arc Model

The entropy production minimization problem of the electric arc, in terms of the arc voltage (V_a in V), the impedance (Z_a in Ω), and the power factor ($\cos\phi$), constitutes an NLP problem. It is presented in Equation (21a)–(21k).

$$\min_{I_a, r_a, T_a} \frac{V_a^2}{Z_a T_a} \cos\phi \quad (21a)$$

$$s. t. \quad \sigma_{\text{mix}}(T_a) - x_C \sigma_C(T_a) - x_{\text{Fe}} \sigma_{\text{Fe}}(T_a) - x_{\text{air}} \sigma_{\text{air}}(T_a) = 0 \quad (21b)$$

$$\begin{aligned} \epsilon_{N_{\text{mix}}}(1 \text{ cm}, T_a) - x_{(0.9 \text{ air} - 0.1 \text{ C})} \epsilon_{N_{(0.9 \text{ air} - 0.1 \text{ C})}}(1 \text{ cm}, T_a) \\ - x_{\text{Fe}} \epsilon_{N_{\text{Fe}}}(1 \text{ cm}, T_a) = 0 \end{aligned} \quad (21c)$$

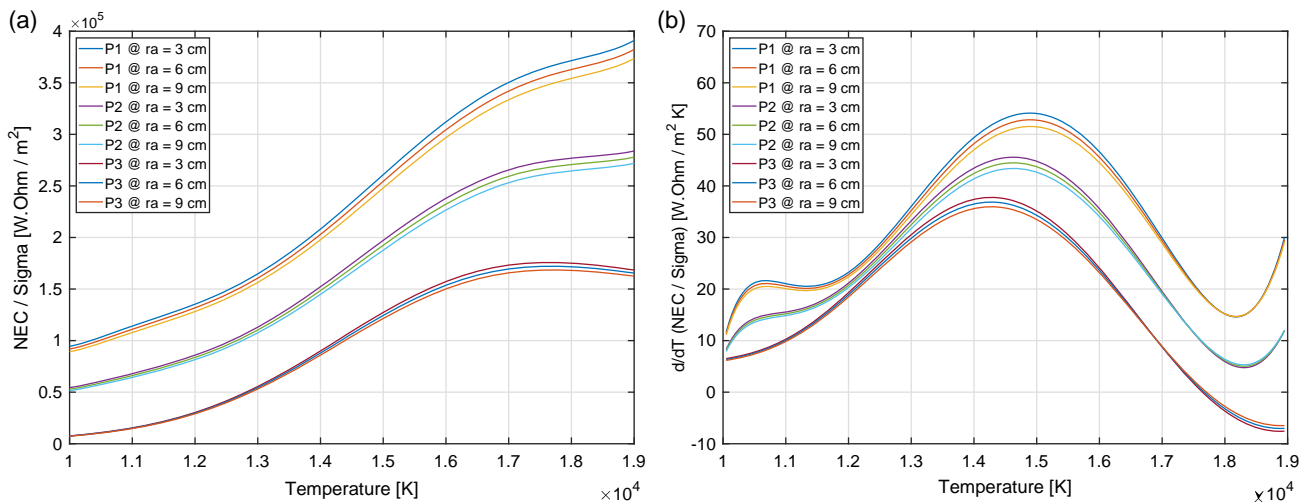


Figure 1. a) γ versus temperature and b) $\frac{d\gamma}{dT}$ versus temperature.

$$\varepsilon_{N_{\text{mix}}}(10 \text{ cm}, T_a) - x_{(0.9 \text{ air}-0.1 \text{ C})} \varepsilon_{N_{(0.9 \text{ air}-0.1 \text{ C})}}(10 \text{ cm}, T_a) - x_{\text{Fe}} \varepsilon_{N_{\text{Fe}}}(10 \text{ cm}, T_a) = 0 \quad (21d)$$

$$\alpha - \frac{1}{9} (r_a - 1) = 0 \quad (21e)$$

$$\varepsilon_{N_{\text{mix}}}(r_a, T_a) - (1 - \alpha) \varepsilon_{N_{\text{mix}}}(1 \text{ cm}, T_a) - \alpha \varepsilon_{N_{\text{mix}}}(10 \text{ cm}, T_a) = 0 \quad (21f)$$

$$4 \pi^2 \varepsilon_{N_{\text{mix}}}(T_a, r_a) r_a^2 l_a - \frac{V_a^2}{Z_a} \cos \phi = 0 \quad (21g)$$

$$\frac{l_a}{\pi r_a^2 \sigma_{\text{mix}}(T)} - Z_a \cos \phi = 0 \quad (21h)$$

$$12\,000 \leq T_a \leq 17\,500 \text{ K} \quad (21i)$$

$$22.6 \leq l_a \leq 57.4 \text{ cm} \quad (21j)$$

$$r_{a_{\text{min}}} \leq r_a \leq r_{a_{\text{max}}} \quad (21k)$$

The origin of the equations is as follows. Equation (21a) is Equation (16), Equation (21b) results from using Equation (17) to estimate the electrical conductivity of the plasma. Equation (21c) and (21d) compute the radiation coefficient of the mixture $\varepsilon_{N_{\text{mix}}}$ at 1 and 10 cm from Equation (17), and Equation (21e)–(21i) are Equation (18), (19), (14), (15), and (20). Boundaries to the radius and length domains were also introduced in Equation (21j) and (21k) to help the solver in search for a global optimum. The bounds to the arc length domain are shown in Equation (21j). They were established using the empirical formula (Equation (37)) provided in Annex B and considering that steel-making arcs operate at voltages between 330 and 700 V. As the value of the arc radius is quite uncertain, varying from 2 to 10 cm,^[7,12,20,30] the bounds of the radius domain were not specified in Equation (21k). Instead, they are treated as parameters which are estimated from the experimental data (see Section 5.1).

4. Experimental Measurements of the Length of Steelmaking Arcs

4.1. General Description

Measuring the length of the electric arc in an operative EAF presents operational and technical challenges. Not only it is difficult to overcome uncontrollable factors like the bending of the arc or the uncertain depth of the depression created by the jet in the liquid metal, but more importantly, the experimental procedures have to be adapted to the state of the melt shop as a fully operative EAF cannot be slowed down or halted.

Two sets of experiments were run in an industrial ultra-highpower EAF (UHP-EAF). In the first set of experiments, the length of the electric arc for a single operative set-point was measured. In the second, the variations of the arc length for various operative set-points were measured. The reasons for having two different experimental procedures are discussed in Section 4.5.

Measurements of the length of the electric arc have been traditionally made raising the electrodes manually from short

circuit (electrode in direct contact with the bath) to arc extinction.^[31] With this dynamic approach, the results for the length of the arc are characterized by considerable variations.^[20,32]

In this work, the length of the electric arc is measured in a static fashion considering the depths of the slag layer and the depression created by the plasma jet. This methodology helps to reduce the arc instabilities that occur in dynamic approaches due to the constant movement of the electrodes. During the computations, the following assumptions are made: 1) the arc behaves as a stabilized column; 2) there is no current flow through the slag; 3) the jet of the arc is sufficiently strong to create a cavity both in the slag layer and in the bath of liquid metal; and 4) the electrodes maintain a fixed position during the experiments. On the basis of these assumptions, the length of the electric arc is estimated as in Equation (22).

$$l_a = l_{a,\text{meas}} + d_{\text{sl}} + n_o \quad (22)$$

where $l_{a,\text{meas}}$ is the measured length of the gap between the electrodes and the slag layer, d_{sl} is the height of the slag layer, and n_o is the depth of the jet depression in the liquid bath.

4.2. Estimation of the Depth of the Slag Layer

The depth of the slag layer is computed as follows: first, the mass of the slag is calculated from the material balance among the initial mass, the mass charged into the EAF, the weight of liquid steel poured out from the furnace at the end of the batch, and the mass that remains in the furnace. The mass loss due to combustion of solid fuels and liquid metal splashing is neglected. Second, the volume occupied by the slag is estimated from the previously calculated mass using a slag density of $(2.7 \pm 0.1 \text{ t m}^{-3})$.^[33] Then the depth of the slag layer can be computed from the area of the flat bath.

4.3. Bath Depression Due to the Jet of the Arc

4.3.1. Shape of the Cavity

In this study, it is assumed that the cavity created by the arc is cylindrical in the slag layer and elliptical in the liquid metal bath. For the case of a thin slag layer, the traditionally assumed half-of-the-cone angle $\beta = 20^\circ$ is used to estimate the radius of the cylindrical cavity in the slag,^[20] see **Figure 2a**. This angle represents the maximum radial deflection that the arc can have due to bending and movements, at any height.

4.3.2. The Force Balance Equation

One way of estimating the depth of the cavity that is created by the electric arc in the pool of liquid metal is to equate the thrust generated by the arc to the gravitational force of the evacuated volume of fluid.^[34,35] For the case of a removed volume composed of slag and liquid metal, the force balance equation reads

$$\frac{\mu_o}{8\pi} I^2 \log\left(\frac{r_a}{r_k}\right) \cos \phi = g d_c^2 \frac{\pi}{4} d_{\text{sl}} \rho_{\text{sl}} + g d_c^2 \frac{\pi}{6} n_o \rho_{\text{mm}} \quad (23)$$

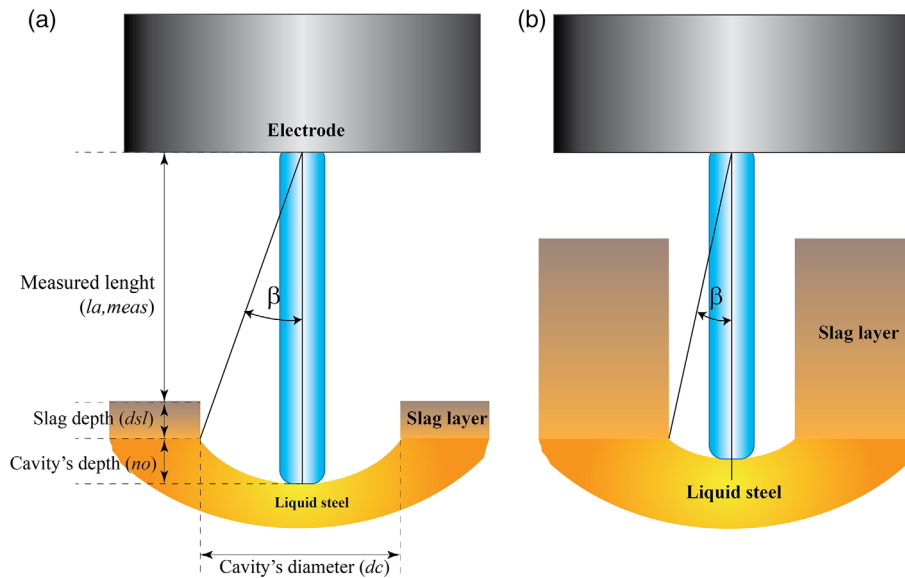


Figure 2. Assumed cavity geometries for a) shallow slag layers and b) deep slag layers.

Here, the left-hand side of the equation represents the corrected thrust generated by an AC arc using Maecker's DC approximation.^[36] While in DC furnaces the electrode operates always as the cathode end of the arc, in an AC furnace, both the electrodes and the metal pool act as cathode ends as the current changes its polarity. Considering that the cavity in the metal pool is created by the downward force of the arc when the electrode acts as the cathode, we approximated the thrust of the AC arc as half of its DC equivalent. The inclusion of the term $\cos\phi$ on the left-hand side of Equation (23) is justified by the fact that only the real component of a complex current performs work in the physical realm.^[23] Equation (23) can be rewritten in the form of the nondimensional diameter-to-depth ratio parameter.^[37,38]

$$\Psi = \frac{d_c}{n_o} = A \sqrt{\frac{\hat{M}}{\lambda n_o^3}} \quad (24)$$

Here, \hat{M} is the thrust responsible for creating the elliptical cavity in the molten metal. Equation (24) establishes a relationship between the magnitude of the force and the geometry of the cavity that it creates in the bath. Based on this parameter, the principle of geometric similarity can be invoked to scale up or down the size of the cavity as the current of the arc is changed. During the experiments, the depth of the cavity created by the jet on the liquid metal was estimated as the following.

1) For shallow slag layers. From Equation (23) and assuming a half-of-the-cone angle of the arc of 20° . See Figure 2a; 2) For deep slag layers. By invoking the principle of geometric similarity and solving Equation (24), assuming the same diameter-to-depth ratio parameter (Ψ) as in the experiments with thin slag layers. See Figure 2b.

Figure 3 shows the values of the diameter (d_c), the depth of the cavity (n_o), and the nondimensional parameter Ψ for the two

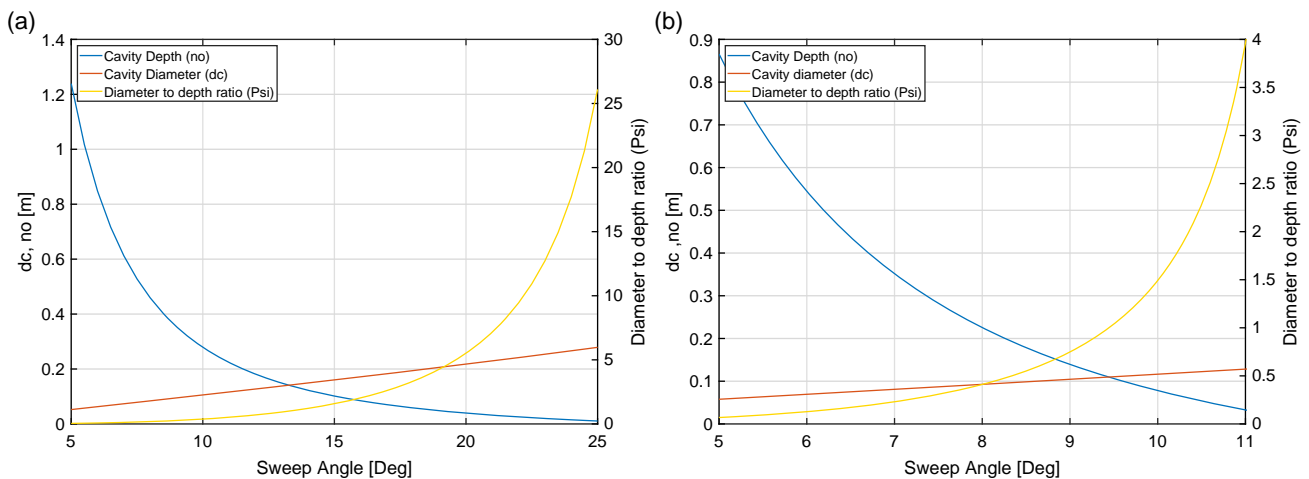


Figure 3. Ψ , d_c , n_o versus half-cone angle (sweep angle), according to Equation (24), for $I = 53.4$ kA, $\rho_{sl} = 2.7$ ton m^{-3} , $\rho_{mm} = 7.0$ ton m^{-3} and a) $d_{sl} = 6.0$ cm and b) $d_{sl} = 31.0$ cm.

estimated slag layers during our experiments ($d_{sl} = 6.0$ cm and $d_{sl} = 31.0$ cm) at various half-of-the-cone angles.

4.4. Arc Length Measurements

4.4.1. Experimental Procedure

For these experiments, a centrally located set-point in the operative domain of the tested EAF that produced a stable electric arc was selected (451 V of 8.45 mΩ). The stability of the arc was evaluated using the empirical criterion that regards an arc as stable if the standard deviation of the current readings remains under 10% of the average value for few seconds.

After selecting an operative set-point, the length of the arc was measured according to the following procedure.

- 1) Under flat bath conditions and before any deslagging operation, an electric arc with the chosen electrical set-point was discharged. After the electric arc stabilized— ≈ 30 s after initial discharge—the electrodes were locked in their position, and the electrical current was interrupted; 2) A marking line was drawn on one of the external support columns of the electrodes at the locked position. See Figure 4a. Then, the marked electrode was slowly lowered until it touched the flat bath, and a new line was drawn on the support column. The lowering process was controlled visually from the slag door using a video camera. Due to the location of the camera, only one electrode could be controlled; 3) The distance between the two markings ($l_{a,meas}$) was measured and used to estimate the length of the electric arc as in Equation (22). See Figure 4b. The precision of this measurement method, in absolute terms, was estimated as ± 2.0 cm because the electrodes couldn't be stopped exactly at the surface of the slag; 4) After measuring the length of the arc, the batch was terminated, the furnace emptied, the mass balances computed, and the depth of the slag layer (d_{sl}) and the depth of the jet depression (n_o) were estimated; 5) The experiment was repeated three times, and the average result was considered as the experimental length of the arc.

4.4.2. Results

Due to production constraints, the experiments were executed in the first and the last batch of a single campaign. Only one experiment was conducted in the first batch. The other two experiments were conducted during the final batch of the campaign. The results of the measurements, along with the computations of the depth of the slag layer and the jet depression, are shown in Table 1.

In Table 1, the statistic bounds correspond to the standard uncertainty of the reported quantity. The errors in the mathematically computed quantities (d_{sl} and n_o) result from the error propagation from the uncertainty in the estimated mass that remains in the furnace and in the uncertainty of the measurements of all: the metal masses, the density of the slag and the electrical current.

For the computation of the arc length according to Equation (22), only the uncertainty associated with the electrical current measurements was Gaussian. The uncertainties associated with the measurement instruments of weight and length as well as that of the approximation of the amount of liquid metal that remains in the EAF after tapping were assumed to have a box distribution.

The depth of the cavity in the molten metal (n_o) for Experiment 1 was estimated as described in Section 4.3.2 procedure 1. For this experiment, the diameter-to-depth parameter was computed with Equation (24) as $\Psi_1 = 5.55$. For experiments 2 and 3, procedure 2 was used. First, the principle of geometrical symmetry was invoked, making $\Psi_1 = \Psi_2 = \Psi_3$, and n_o for Experiments 2 and 3 was computed solving Equation (24).

Table 1. Experimental results for the reference arc (451 V and 8.45 mΩ).

Arc	$l_{a,meas}$ [cm]	d_{sl} [cm]	n_o [cm]	l_a [cm] from Equation (32)
Experiment 1	24.0 ± 1.2	5.9 ± 0.2	4.0 ± 0.5	33.9 ± 1.3
Experiment 2	3.0 ± 1.2	31.0 ± 1.0	2.4 ± 0.4	36.4 ± 1.6
Experiment 3	2.0 ± 1.2	31.0 ± 1.0	2.4 ± 0.4	35.4 ± 1.6

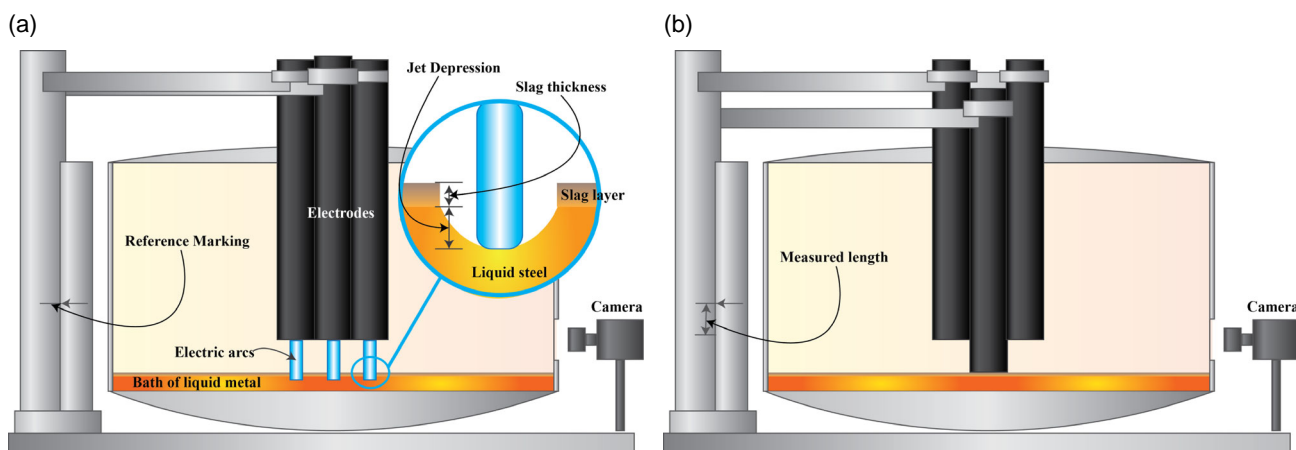


Figure 4. Experimental procedure to measure the arc length. a) Arc discharge and reference line. b) Electrode lowered and measured distance.

The estimated Ψ is in agreement with the experimental values reported in earlier studies.^[39,40] The previous computations suggest that the depth of the depression in the liquid metal bath created by the jet of the arc decreases as the slag layer increases. More precisely, the depth of the cavity is reduced by $\approx 35\%$ as the arc coerture by the slag increases from 30% to 92%.

The length of the electric arc at the test conditions of 451 V of 8.45 m Ω is computed as the average of the arc lengths in Experiments 1–3:

$$l_a = \frac{l_{a,1} + l_{a,2} + l_{a,3}}{3} = 35.2 \pm 0.9 \text{ cm} \quad (25)$$

4.5. Experiments with Different Electrical Settings

4.5.1. Experimental Procedure

The experimental procedure in the previous section had to be changed as it extended the processing time of a single batch by over 15 min, which is unacceptable during normal operations. One way to overcome this problem is to carry out the measurements of the length of the arc in a differential fashion with respect to a reference arc and on the three electrodes simultaneously.

The idea behind the differential arc length experiments is to analyze how the length of the arc varies with the voltage at two different impedance levels: 6.0 and 8.45 m Ω . These two impedance levels were chosen because in the studied EAF, they also lead to stable arcs. At these two impedance levels, two points with significantly different voltages were chosen. In practice, it is not possible to operate at any desired voltage or impedance level. From the range of available set-points, those that enabled large-voltage excursions with minimal deviations from the selected impedance levels were [500 V, 8.55 m Ω], [400 V, 8.20 m Ω], [451 V, 6.25 m Ω], [400 V, 6.00 m Ω].

The arc length variations were measured according to the following procedure.

1) During flat bath conditions and before any deslagging, the reference electric arc with the voltage and impedance set-point of 451 V and 8.45 m Ω was discharged; 2) Following the stabilization of the arc, the electrodes were locked in their position, the electrical current was interrupted, and a marking line was drawn on the three external support columns of the electrodes; 3) After marking, the electrodes were released, and a second arc with one of the earlier-mentioned set-points was discharged; 4) After the stabilization of the second arc, the electrodes were locked in their new position, the electrical current was interrupted, and a second marking was made on the three support columns; 5) For all three phases, the distances between the two markings were measured ($l_{a,\text{meas}1,2,3}$) and taken as the change of the arc length with respect to the reference arc.

It follows from Equation (22) that the differential arc length between the second and the first discharged arcs is

$$\begin{aligned} \Delta l_a &= (l_{a,\text{meas}2} - l_{a,\text{meas}1}) + (d_{\text{sl}2} - d_{\text{sl}1}) + (n_{\text{o}2} - n_{\text{o}1}) \\ &= l_{\Delta,1,2,3} + \Delta d_{\text{sl}} + \Delta n_o \end{aligned} \quad (26)$$

Here, $l_{\Delta,i}$ is the measured distance in each phase of the EAF (1, 2, 3) and $\Delta d_{\text{sl}} = 0$ because the slag depth for both arcs is the

same. As these experiments were conducted in the early batches of various productions campaigns (as Experiment 1), we assumed $n_{\text{o}1} = 4.0 \pm 0.5$ cm. $n_{\text{o}2}$ was estimated using Equation (24), and invoking the principle of geometrical symmetry for the same diameter-to-depth ratio as before, $\Psi = 5.55$. The length of the second discharged arc can be computed as

$$l_{a,i} = l_{a,\text{ref}} + \Delta l_{a,i} = l_{a,\text{ref}} + l_{\Delta,i} + \Delta n_o \quad (27)$$

In Equation (27), $l_{a,\text{ref}}$ is the average length of the arc of Experiments 1–3 computed in Equation (25), and Δn_o is the same for the three phases because the variation of the mean of the current readings among the three phases is small. Finally, the length of the arc for the differential experiment is estimated as the average arc length of the three phases.

4.5.2. Results

The readings of each measured delta $l_{\Delta,i}$ as well as the computations of each depth of the cavity (Δn_o) and the length of the arc are shown in **Table 2**, where all the statistic bounds correspond to the standard uncertainty of the reported quantity.

Figure 5a shows the trends for the arc length versus the voltage at the selected impedance levels. **Figure 5b** shows the arc length versus the impedance, at the two studied voltage levels (400 and 450 V). The error bars represent the 95% confidence interval of the measurement (standard uncertainty multiplied by a coverage factor $k = 2$).

The line of best fit (LOBF) in **Figure 5a,b** suggests that the length of the arc can be increased either by raising its voltage, its impedance, or both. At the same voltage level, arcs with a larger impedance set-point are also longer. In a similar fashion, higher-voltage levels promote longer arcs at the same impedance level.

5. Numerical Results and Discussions

5.1. Determination of the Bounds and of the Radius of the Arc

Due to the nonconvex nature of the NLP (Equation (21a)–(21k)), the problem was implemented in GAMS and solved using the

Table 2. Experimental results for the different settings.

Arc	Electrode	$l_{a,\text{ref}}$ [cm]	$l_{\Delta,i}$ [cm]	Δn_o [cm]	$l_{a,i}$ [cm]	l_a [cm]
Experiment 4	1		-1.5 ± 1.7	0.3 ± 0.8	34.0 ± 2.1	36.3 ± 1.2
	2		3.0 ± 1.7		38.5 ± 2.1	
	3		1.0 ± 1.7		36.5 ± 2.1	
Experiment 5	1	35.2 ± 0.9	-5.0 ± 1.7	-0.3 ± 0.7	29.9 ± 2.0	31.6 ± 1.2
	2		-2.0 ± 1.7		32.9 ± 2.0	
	3		-3.0 ± 1.7		31.9 ± 2.0	
Experiment 6	1		-6.5 ± 1.7	1.0 ± 0.9	29.7 ± 2.1	30.1 ± 1.2
	2		-6.3 ± 1.7		29.9 ± 2.1	
	3		-5.5 ± 1.7		30.7 ± 2.1	
Experiment 7	1		-10.0 ± 1.7	0.7 ± 0.9	25.9 ± 2.1	27.4 ± 1.2
	2		-8.5 ± 1.7		27.4 ± 2.1	
	3		-7.0 ± 1.7		28.9 ± 2.1	

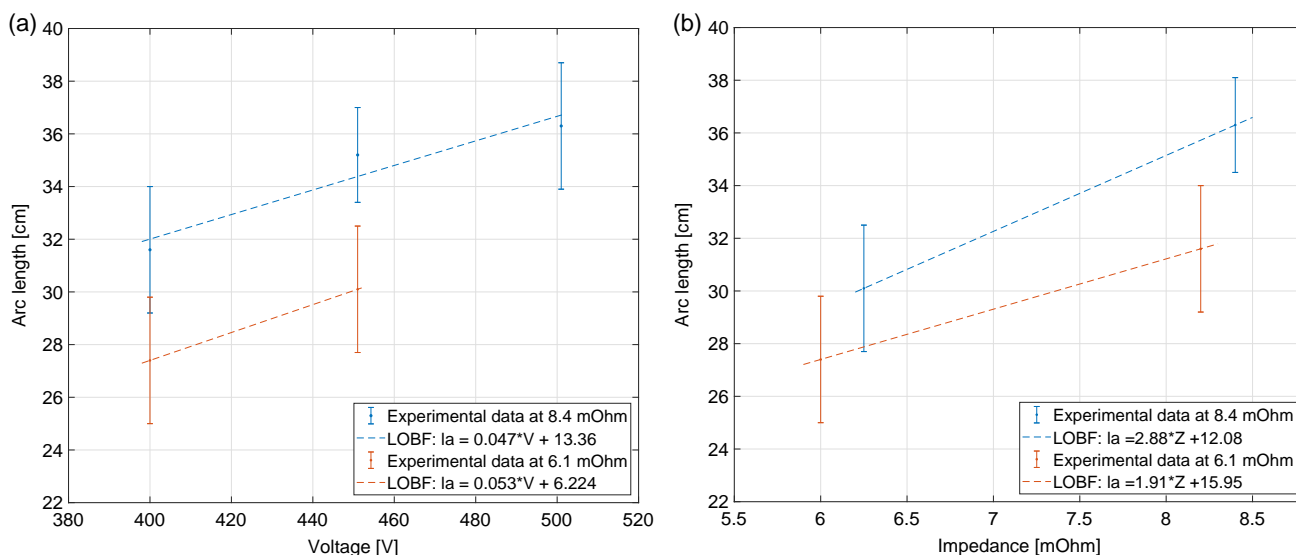


Figure 5. Results of the Experiments 4 to 7. a) Arc Length vs Voltage at two impedance levels. b) Arc length vs impedance at two voltage levels.

BARON global solver.^[41,42] For the electrical set-point of the reference arc described in our experimental section ($V_a = 451$ V and $Z_a = 8.45$ m Ω), the model was solved, reducing the value of $r_{a,min}$ from 8 to 2.5 cm, for the plasma compositions P1, P2, and P3. In all the cases, the value of the upper bound $r_{a,max}$ was set to the maximum value reported in the literature, 10 cm. The results of these computations are shown in **Figure 6**.

As $r_{a,min}$ is reduced from 8 to 2.5 cm, there are three possible solution scenarios to the NLP problem. In the first, for values of $r_{a,min}$ that are between 8.0 and 5.5 cm for P1, between 8.0 and 6.0 cm for P2, and between 8.0 and 7.0 cm for P3, the physical relations of the plasma are not satisfied, and the solver reports infeasibility. In Figure 6a–c, the nonfeasibility situation is presented as 0 in the curves for P1, P2, and P3. As $r_{a,min}$ is further reduced and the problem has a solution, a second region where the radius of the arc is always equal to $r_{a,min}$, for all the plasmas, appears. This second region ranges from ≈ 6.0 to 4.0 cm (see Figure 6b). Finally, two cases can occur as $r_{a,min}$ is further decreased below 4.0 cm. Either the temperature reaches the upper bound of the temperature domain (see Figure 6c from 3.5 to 2.5 cm for P3) or the problem becomes constrained

by the lower bound of the arc length domain (see Figure 6a from 3.5 to 2.5 cm for P1 and P2). Interestingly, once the arc becomes bounded by its temperature or by its length, further reductions in $r_{a,min}$ have no impact on its geometry.

The effect of $r_{a,min}$ on the solution reported by the solver can be better understood in **Figure 7**, where a 3D representation of the solution space of the NLP for the plasma P3 is shown. As $r_{a,min}$ is changed (moved), the solution point reported by the solver also changes because its location is determined by the intersection of the hyperplanes created by the entropy, $r_{a,min}$, and the Elenbaas–Heller and Ohm’s law equations.

Considering that the solver will terminate at a point that depends on the chosen value of $r_{a,min}$, and that the composition of the plasma plays also a key role in its final geometry and temperature (see from Figure 6a–c), a parameter estimation technique is utilized to compute their optimal values. To this aim, the root mean squared error (RMSE) [Equation (28)] between the average value of the length of the experimental arcs in Section 4 and the values predicted by the NLP is minimized using a univariate sensitivity analysis methodology.

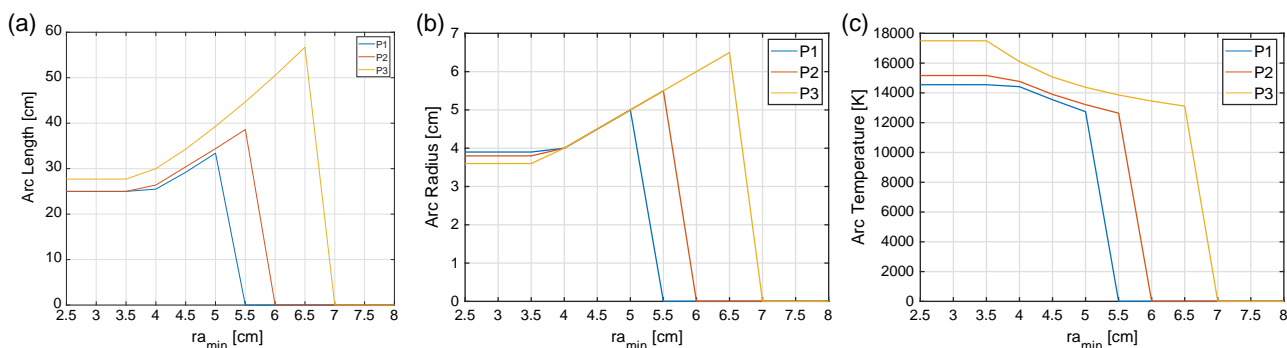


Figure 6. Parametric study of the solution point of the NLP in terms of $r_{a,min}$ assuming $\cos = 0.8$. a) Arc length (l_a) vs. $r_{a,min}$. b) Arc radius (r_a) vs. $r_{a,min}$. c) Arc temperature (T_a) vs. $r_{a,min}$.

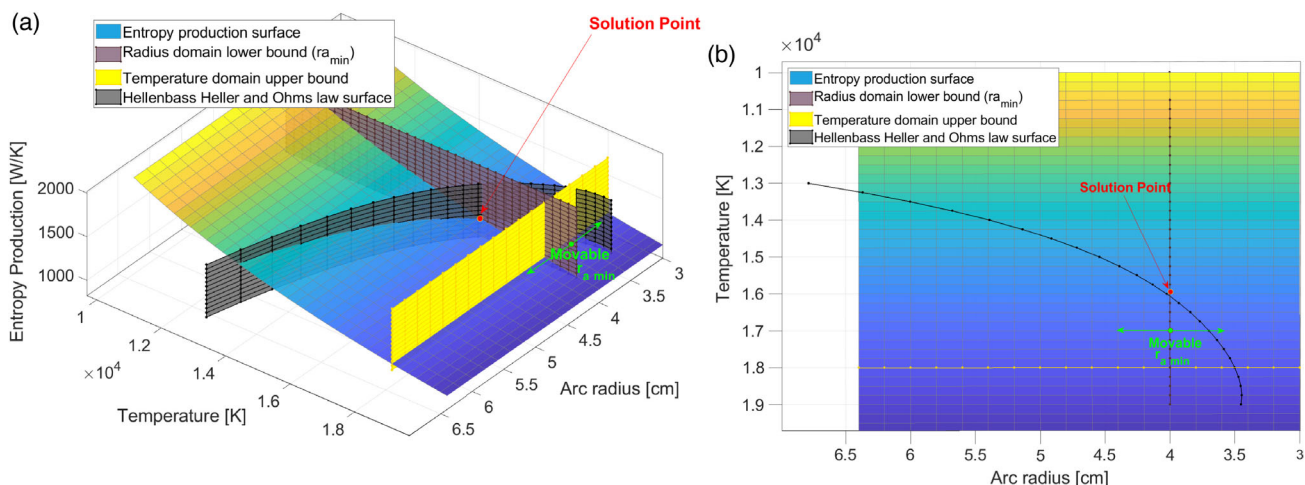


Figure 7. Solution space of the NLP. a) Hyperplanes for the reference arc ($V = 451$ V and $Z = 8.45$ m Ω). b) Top view of (a).

$$RMSE = \sqrt{\frac{1}{N} \sum_{k=1}^N (I_{a,meas}(V_k, Z_k) - I_{a,NLP}(V_k, Z_k, r_{a_{min}}))^2} \quad (28)$$

for P1, P2, and P3

Because the value predicted by the NLP will depend on both the assumed value of $r_{a_{min}}$ and the plasma composition, Equation (28) is solved for various values of $r_{a_{min}}$ from 3.8 to 5.5 cm, in steps of 1 mm, for the three plasma compositions P1, P2, and P3. The results of these computations are shown in **Figure 8**.

Figure 8 shows that the optimal values of $r_{a_{min}}$ for P3, P2, and P1 are 4.5, 5.0, and 5.2 cm. Also, the minimum value of the RMSE is approximately the same (0.5 cm) for the three plasmas. The optimal value of $r_{a_{min}}$ depends on the iron content of the mixture. As iron is added to the plasma, the radius of the arc also increases.

A series of additional computations for plasmas with iron compositions of 12% and 15% were performed and it was found out that for these cases the NLP solver reported infeasibility. This occurs because as more iron is added to the plasma, the

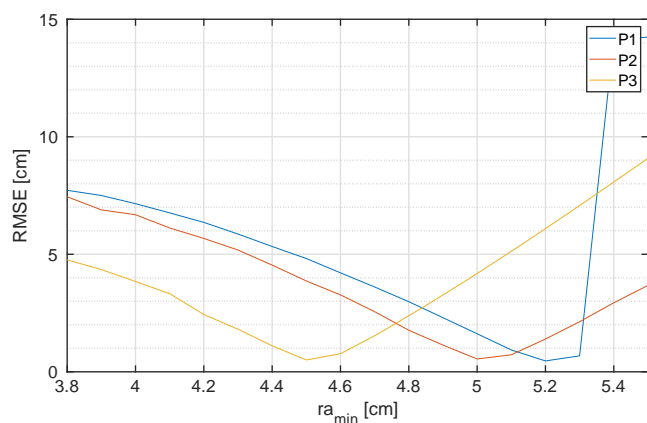


Figure 8. RMSE at various values of $r_{a_{min}}$.

temperature at which the radiation mechanisms equate the heating mechanisms decreases and eventually drops below the feasible region. The equilibrium temperature at the optimal $r_{a_{min}}$ for each plasma composition and for each of the experimental arcs is shown in **Figure 9**.

The results in Figure 9 show that the addition of iron leads to colder arcs, regardless of the electrical set-points. On the other hand, arcs at higher impedance levels also produce colder arcs at the same voltage level, and arcs at higher voltage levels are hotter at the same impedance level, independent of the composition of the plasma. These findings suggest that in the operational domain of an EAF, for a desired power level, the coldest arc will occur for the electrical set-point with the largest impedance and the lowest voltage. This observation serves as a decision criterion to select the most likely plasma composition for the NLP model: the selected plasma composition must provide feasible solutions for all possible combinations of voltage and impedance set-points in the operative domain (infeasibilities are most likely to occur due to violations

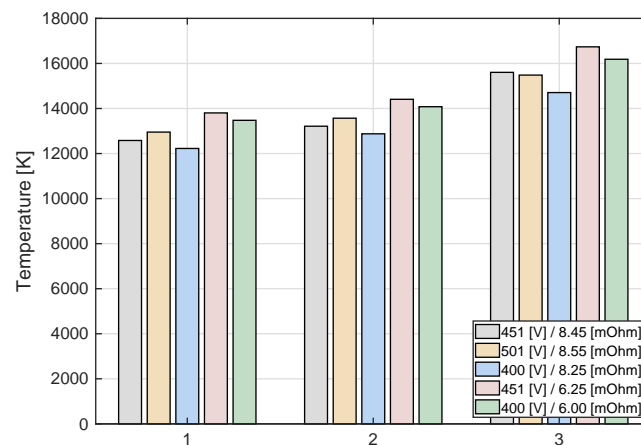


Figure 9. Plasma temperatures for the five experimental arcs at the optimal $r_{a_{min}}$ values for the three plasma compositions P1 (1), P2 (2), and P3 (3).

of the lower bound of the temperature domain at 12 000 K). As the temperature of the arc decreases as its iron content increases, the appropriate plasma composition is that with the largest amount of iron and for which the NLP reports a feasible solution at the electrical set-point, producing the coldest arc (lowest power level and the highest impedance level).

In **Figure 10**, the feasible operational domain of an UHP-EAF is presented. From this, one can conclude that the extreme point at which the analysis of the plasma composition must be conducted is 450 V and 11.5 mΩ.

At this electrical set-point, the NLP reported feasible solutions only for P3 and P2. Considering that P3 represents an arc with no added iron, one can conclude that P2 is a suitable plasma composition to model the electric arc in the tested EAF. For P2, $r_{a,min} = 5.0$ cm provides the best fit to the experimental data (**Figure 8**).

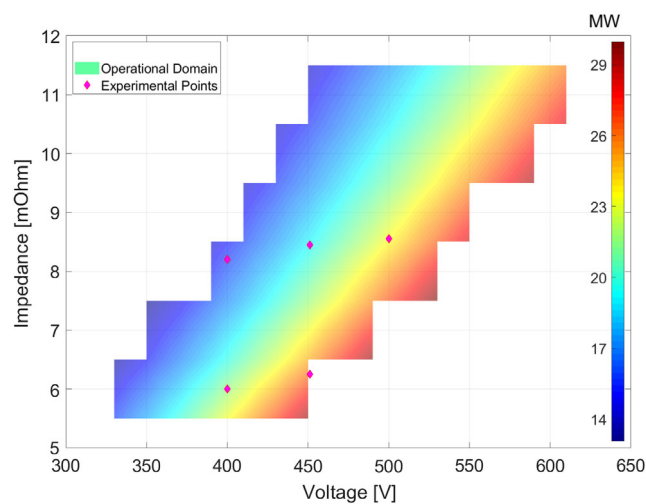


Figure 10. Operative domain of the arc in an UHP-EAF.

5.2. Voltage and Impedance Effects on the Length of the Arc

In this subsection, the influence of the voltage and impedance set-points on the length of the electric arc is investigated numerically. Assuming a plasma composition as in P2, $r_{a,min} = 5.0$ cm and $\cos\phi = 0.8$; the NLP was solved varying the voltage set-point of the arc from 330 to 630 V, in 20 V steps, at fixed impedance levels of 11.5, 10.5, 9.5, 8.5, 7.5, 6.5, and 5.5 mΩ. The results of these computations are shown in **Figure 11**. The analysis is limited to the operational domain shown in **Figure 10**.

Figure 11a,b show that a) the length of the arc increases as the voltage and impedance set-points are raised. At a single impedance level, larger voltages lead to longer arcs, and at the same voltage level, impedance increments lead to also longer arcs. b) Despite the highly nonlinear nature of the physics of the arc, the correlation between the length of the arc and its voltage and impedance set-points is nearly linear in the analyzed domain.

As a result, we propose to compute the length of the arc (l_a) as a linear combination of two linear terms, one depending on the voltage and the other on the impedance:

$$l_a = m_V V_a + m_Z Z_a \quad (29)$$

Here, m_V and m_Z are the numerically estimated coefficients that represent the gradients with respect to voltage and impedance. They are given in cm/V and cm/mΩ. The operative set-points of the arc V_a and Z_a are given in V and mΩ and the arc length l_a in cm.

5.3. The Proposed Linear Approximation

The coefficients m_V and m_Z in Equation (29) were computed by linear regression using the 63 points shown in **Figure 11**. The result of this computation is

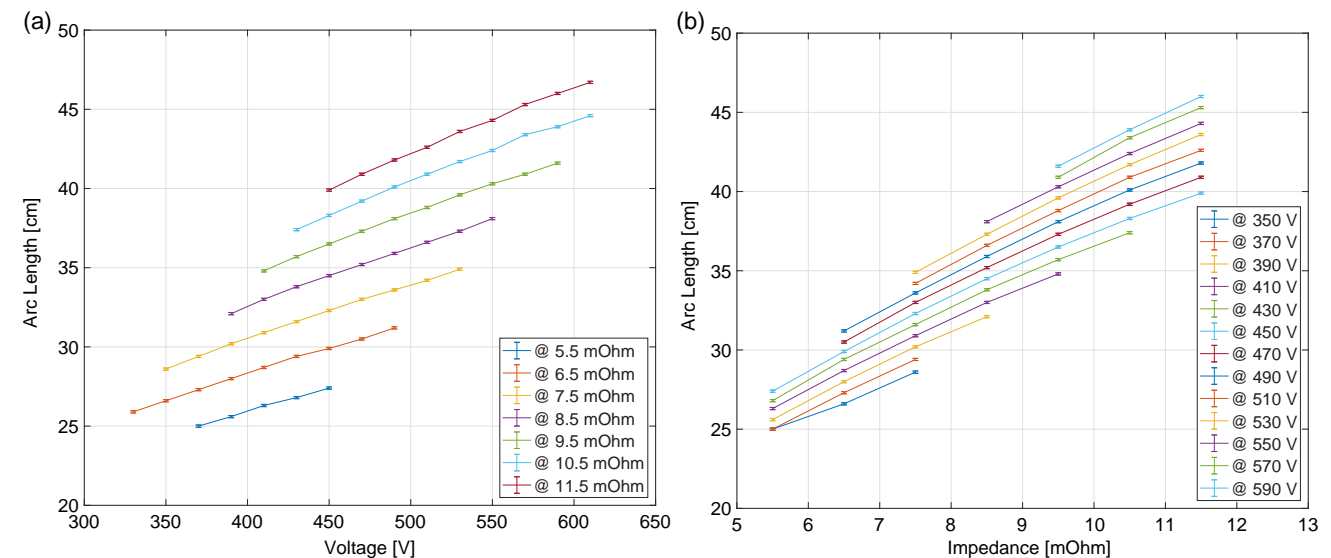


Figure 11. Predicted influence of the voltage and impedance set-points on the length of the arc. a) Arc length vs. arc voltage. b) Arc length vs. arc impedance.

$$l_a = 0.037 V_a + 2.112 Z_a \quad (30)$$

With the aim of providing a simplified formula that is easy to memorize and that can help operators to quickly compute the length of the arc during operations, Equation (30) was rearranged and its coefficients were rounded up to the nearest integer. One obtains a simple formula.

$$l_a = \frac{V_a + Z_a a}{b}, \quad \text{with } a = 57 \text{ and } b = 27 \quad (31)$$

In **Figure 12**, the resulting surfaces from interpolating the results of the NLP throughout the operative domain as well as that of the plane created by Equation (31) are presented. The experimental measurements of the length of the experimental arcs are also added. The three diamonds in each group represent the mean and the 95% confidence intervals of the measurements of the arcs in the Experimental Section.

These results clearly show that the developed models predict remarkably well the length of the experimental arcs. For all the experimental arcs, the predictions obtained from the NLP and the linear formula almost intersect the mean value of the measurements. Figure 12b shows that the surface that is created by the highly nonlinear NLP is approximated well by the linear plane (Equation (31)) in the analyzed domain.

5.4. Effects of the Voltage and Impedance Set-Point on the Temperature of the Arc

Under the assumption that the arcs have a radius equal to 5.0 cm, for a given pair of voltage and impedance set-points, the temperature of the arc can be estimated directly from Ohm's law without the need of solving the NLP. Assuming $\cos\phi = 0.8$, and substituting Equation (31) into Equation (15), one obtains the following implicit formula for the estimation of the temperature of the electric arc.

$$\sigma(T_a) b = a + \frac{V_a}{Z_a}, \quad \text{with } a = 57 \text{ and } b = \frac{54 \pi}{10000}. \quad (32)$$

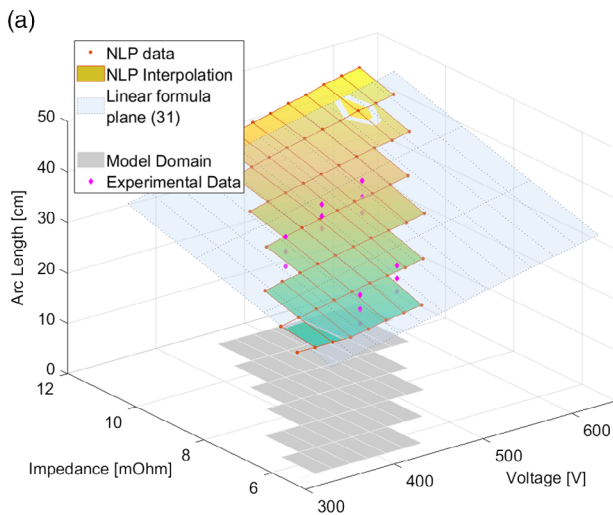


Table 3. Estimated arc temperatures and errors, NLP versus the result from Equation (32).

Experiment	Arc temperature NLP [K]	Arc temperature (Equation (42)) [K]	Abs. error [%]
Reference	13 213	13 235	0.2
Test 4	13 569	13 607	0.3
Test 5	12 876	12 908	0.2
Test 6	14 408	14 580	1.2
Test 7	14 079	14 185	0.8

Here, V_a , Z_a , and T_a are given in V, $m\Omega$, and K. The temperature of the five experimental arcs was computed using the NLP and by solving numerically Equation (32). The results are shown in **Table 3**.

The results in Table 3 demonstrate that Equation (32) predicts the temperature of the arc well and with a maximum error of 1.2%. The results of these temperature computations align well with the temperatures reported in the MHD studies of electric arcs carrying similar levels of electrical current.^[30,43,44]

6. Comparison of the Results with Other Models

In this section, the performance of the models presented here is compared with those of the empirical formula (Equation (37))^[45] and the implicit formula (Equation (36)) proposed by Bowman.^[7] An overview of these two models is provided in Annex B. Using the experimental data in Section 4 as a benchmark for comparison, the RMSE between the predictions made by various models and the measured arc lengths in Table 2 is estimated. Considering that both the empirical and Bowman's model rely on assumed or estimated parameters, for the sake of a fair comparison, the free parameters of these models are also estimated using the available experimental data. All RMSEs are computed with respect to the mean value of the experimental measurements.

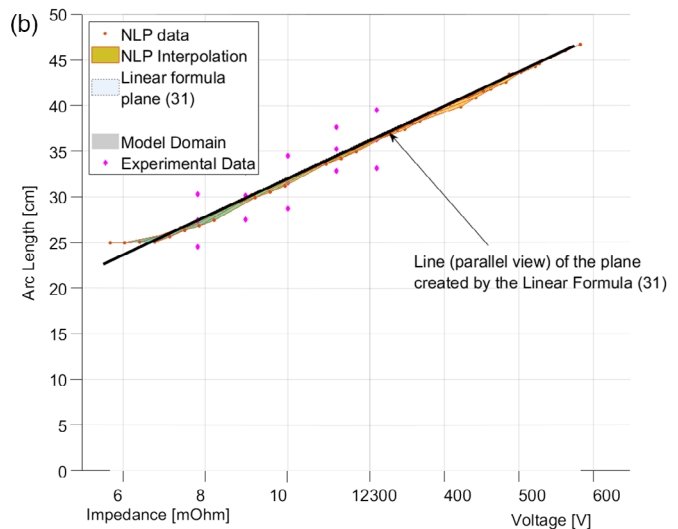


Figure 12. NLP surface, linear formula plane, and experimental measurements. a) Isometric view of the surfaces. b) Rotated view of (a).

6.1. Empirical Formula

In the industry, the length of the electric arc has traditionally been estimated using the empirical formula (Equation (37)) provided in Annex B. This arc model depends on two parameters: the voltage drop at the anode and cathode ends of the plasma V_{an_ca} and the magnitude of the electric field in the column. Although the value of these parameters can vary largely from melt shop to melt shop, normally accepted values are $V_{an_ca} = 40.0 \text{ V}$ and $E_{arc} = 11.5 \text{ V cm}^{-1}$.^[45] The performance of this formula can be evaluated in terms of the RMSE either by using these values or by estimating them from our experimental data, making use of Equation (28). For the second approach, the obtained vector of the estimated parameters is $V_{an_ca} = -38.7 \text{ V}$ and $E_{arc} = 14.9 \text{ V cm}^{-1}$. The RMSE for both cases is shown in Table 4.

6.2. Bowman's Formula

In the same fashion as for the empirical formula, the performance of the adjusted and the nonadjusted Bowman's formula is measured with the RMSE of the predictions of the models with respect to the experimental data. In his work, Bowman used a linear approximation of the electrical conductivity of a plasma containing 25% carbon, 10% iron, and 65% air and assumed a current density at the cathode spot and an arc temperature of 3500 A cm^{-1} and $15\,000 \text{ K}$.^[7] Here, these two parameters were adjusted using a nonlinear parameter estimation technique which aimed at minimizing the RMSE between the prediction of the adjusted model and the experimental data. In these computations, the same polynomial approximation of the plasma conductivity as in the NLP model for P2 was used. Furthermore, the current in the formula was also corrected by the $\cos\phi = 0.8$ factor, linking the physical phenomena to the real component of the AC current. The solution domain of the temperature was constrained as in the NLP model ($12000 \leq T_a \leq 17500 \text{ K}$) and the current density between values reported in the literature ($2500 \leq J_k \leq 4500 \text{ A cm}^{-1}$). The error for the nonadjusted model was computed using the original values of the parameters and the original linear approximation for the conductivity of the plasma. The results of the error calculations are shown in Table 5.

Table 4. RMSE for the empirical formula for standard values^[45] and for estimated values of V_{an_ca} and E_{arc} .

Method	$V_{an_ca} [\text{V}]$	$E_{arc} [\text{V cm}^{-1}]$	RMSE [cm]
Nonadjusted	40	11.5	5.6
Adjusted	-38.7	14.9	2.1

Table 5. RMSE for the various cases of the Bowman's formula.

Method	$T_a [\text{K}]$	$J_k [\text{A cm}^{-1}]$	$\sigma(T)$	RMSE [cm]
Nonadjusted	15 000	3500	Original linear	15.4
Adjusted	17 500	3295	Polynomial for P2 (Annex A.)	2.6

The results in Table 5 demonstrate that also for the widely accepted Bowman model, the error of the predictions can be quite large if the model is not adjusted to the specific operative conditions of the EAF.

6.3. NLP and Linear Formula

In Table 6 and Figure 13, the arc length predicted by each method of computation of the length of the electric arc is compared. Here, the statistic bounds in the value of the experimental arcs correspond to the expanded uncertainty multiplied by a coverage factor $k = 2$, providing a level of confidence of $\approx 95\%$. For these comparisons, only the adjusted models of the empirical formula and Bowman's formula are considered.

For each model prediction l_{amodel} , the relative absolute error with respect to the mean value of the measurement l_a in Table 2 was computed as

$$\text{err}_{\text{abs}} = \left\| \frac{l_a - l_{amodel}}{l_a} \right\| * 100\% \quad (33)$$

The results of these computations are shown in Figure 14.

The results in Table 6 show that for the tested arcs, the models presented here outperform other state-of-the-art methods for the estimation of the length of the arc, in terms of both the overall RMSE and for most of the individual cases. In Figure 14, the relative absolute errors in the predictions of the different models, according to Equation (33), are shown. While the maximum error of the predictions of the NLP and the proposed linear formula is $\approx 3\%$, the errors of the empirical formula and of Bowman's model are 9% and 12%. While the predictions of our models are characterized by a constant error over the whole domain, the error of the other models varies considerably from one point to another. For example, Bowman's model predicts the length of the electric arc best in the middle of the operative range of the voltage, around 450 V. For higher- or lower-voltage values, the error in Bowman's predictions grows considerably and can reach values of $\approx 12\%$, which is the largest among all the models.

The results in Table 6, Figure 13, and 14 suggest that the fitted empirical formula performs better than the fitted Bowman's formula in terms of the RMSE. Interestingly, this occurs even though the empirical formula falls short at describing the effect of the impedance set-point on the length of the electric arc. For all the experimental arcs, the predictions of the NLP and the linear formula lie almost at the center of the confidence interval of the measurement, and those obtained using the empirical formula and Bowman's formula lie for most of the cases at the limit or just outside the confidence interval.

The results in Table 6 also suggest that the linear formula predicts the length of the experimental arcs slightly better than the NLP. This result was explored in more depth by computing the zeta score (Z) between the predictions of the two models with respect to the standard uncertainty in the measurement $u(l_a)$.

Table 6. Predictions of the different arc length computation methods.

Experiment	l_a [cm]	NLP (Equation (21)) [cm]	Linear formula (Equation (31)) [cm]	Empirical adjusted (Equation (37)) [cm]	Bowman adjusted (Equation (36)) [cm]
Reference	35.2 ± 1.8	34.4	34.5	32.8	34.8
Experiment 4	36.3 ± 2.4	36.4	36.6	36.1	40.5
Experiment 5	31.6 ± 2.4	32.0	32.1	29.4	28.8
Experiment 6	30.1 ± 2.4	29.3	29.9	32.8	30.1
Experiment 7	27.4 ± 2.4	27.2	27.5	29.4	24.5
RMSE [cm]	–	0.5	0.4	2.1	2.6

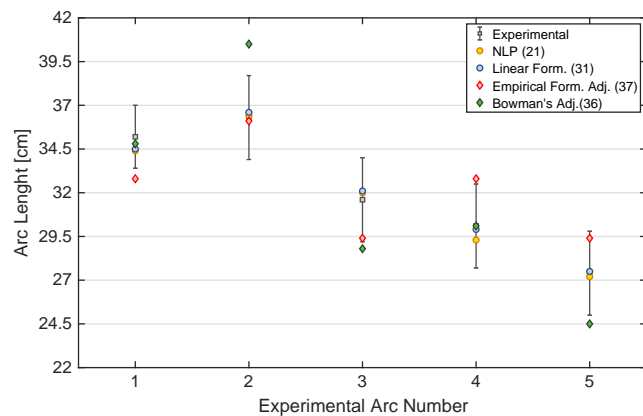


Figure 13. Numerical versus experimental results. 1-Reference, 2-Test 4, 3-Test 5, 4-Test 6, 5-Test 7.

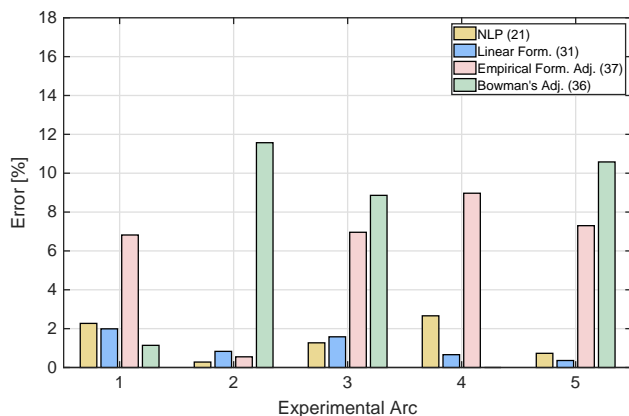


Figure 14. Errors in the predictions of the models according to Equation (33). 1-Reference, 2-Test 4, 3-Test 5, 4-Test 6, 5-Test 7.

$$Z = \left\| \frac{l_{a\text{NLP}} - l_{a\text{linearformula}}}{u(l_a)} \right\| \quad (34)$$

For all the cases, a maximum zeta score of 0.5 was obtained. Because Z is always lower than 2, one can conclude that the difference between the predictions of the two models is insignificant, implying that, from a statistical point of view, the predictions of the linear formula are as good as those of the NLP.

7. Conclusion

In this article, an implicit electric arc model that predicts the length and the temperature of a steelmaking electric arc was presented and successfully validated. The implicit NLP model uses the principle MinEPP, the Elenbass–Heller equation, and Ohm’s law to predict the steady state of a steelmaking arc. The result depends on the constraint on the radius and the assumed composition of the plasma. It was found that the NLP provides the best prediction of the geometry of various steelmaking arcs if the lower bound of the radius was set to 5.0 cm. Furthermore, it was estimated that the composition of a steelmaking arc is $\approx 9.3\%$ carbon, 6.5% iron, and 84.2% air. The results of these simulations also suggest that it is very unlikely for an electric arc in steelmaking to have a radius above 7.0 cm at power levels from 15 to 30 MW.

The influence of the voltage and impedance set-points of the arc on its length was studied extensively. The results of the simulations conducted here suggest that despite the highly nonlinear nature of the problem, the relationship between the voltage, the impedance, and the length of the electric arc can be assumed as linear. Based on these results, a simplified linear formula that predicts the length of the arc in terms of its voltage and impedance set-points was proposed, and the rate of change of the length of the arc with respect to its impedance set-point was calculated (which is $\approx 2 \text{ cm m}\Omega^{-1}$). Furthermore, it was demonstrated that the temperature of the steelmaking arc can also be estimated by solving a relatively simple implicit equation, yielding a maximum error of 1.2% with respect to the temperature computed by the NLP.

The length of various electric arcs under real operative conditions was successfully measured in a fully operative UHP–EAF. The estimations relied on the computations of the depth of the slag layer and the depth of the cavity created by the arc in the liquid bath. While the first was estimated quite accurately from process data, the second required a set of assumptions regarding the geometry of the cavity and the physically possible value of the sweep angle of the arc.

The results of this study can serve as a starting point in the development of more elaborated MHD models where the definition of appropriate boundary and initial conditions is critical to the convergence of the solver. An advantage of using the simplified model presented here is that it predicts arc geometries that implicitly satisfy the steady-state condition of MinEPP and the conditions for the LTE assumption to hold. Furthermore, the

proposed formulae for the estimation of the length and the temperature of the arc can help to better describe the melting process of the EAF, as they can easily be integrated in EAF process models. This can help researchers to understand how a given voltage and impedance set-point influences the temperature and the geometry of the arc, which, until now, are core assumptions in many EAF process models.^[46–51]

It was demonstrated that for various operative conditions, the models proposed here predict the length of the arc better than the widely accepted empirical formula (Equation (37)) and the well-known Bowman's formula (Equation (36)). The errors in the estimation of the length of the arc using the proposed models were smaller than 0.5 cm.

Considering that the core of the arc model is an energy balance between the electrical power input to the arc and the heat loss via radiation mechanisms only, our results can also serve as supporting evidence to the hypothesis that radiation is the

predominant mechanism of energy transfer in a steelmaking arc. This implies that in the EAF process model, the heat exchange from the arc to the other surfaces in the EAF enclosure can be modeled by considering radiation only. In other works, we have developed such a model and will use it to optimize the operation of the EAF with respect to the consumption of electric power.

Annex

Annex A. Polynomial Approximations to the Plasma Properties

The polynomial approximations of the electrical conductivity of air, iron, and carbon plasmas are shown in **Table 7**.

The polynomial approximations of the NEC coefficient of iron and air-carbon plasmas are shown in **Table 8**.

Table 7. Electrical conductivity of air, iron, and carbon plasmas $\sigma(T)$.

	$\sigma_{\text{air}}(T)$	$\sigma_{\text{Fe}}(T)$	$\sigma_{\text{C}}(T)$
a_8	8.0612316E-02	4.3591651E-01	-1.1105338E+00
a_7	-4.5494997E+00	4.8854437E-02	1.8643252E+01
a_6	9.0656657E+00	7.9932799E+00	1.7006116E+01
a_5	4.1157708E+01	5.0707513E+00	-1.7872892E+02
a_4	-8.1652586E+01	6.0500562E+01	3.0746339E+02
a_3	-1.1878766E+02	2.0535827E+01	1.9076191E+02
a_2	-2.6006224E+01	-4.9227842E+02	-8.6371959E+02
a_1	2.3591301E+03	7.9550125E+02	2.8164225E+03
a_0	7.6300402E+03	8.2093344E+03	4.4714539E+03
a_m	1.4500000E+04	1.4500000E+04	1.1123623E+04
a_s	2.6413380E+03	2.6413380E+03	4.2280000E+03

$x = \frac{T-a_m}{a_s}, T$ in K

$\sigma_x(T) = a_8 x^8 + a_7 x^7 + a_6 x^6 + a_5 x^5 + a_4 x^4 + a_3 x^3 + a_2 x^2 + a_1 x + a_0, \sigma_x(T)$ in $\Omega^{-1} \text{ m}^{-1}$

Table 8. NEC of iron and carbon-air plasmas $\epsilon_N(T)$.

	$\epsilon_{\text{NFe}}(r_a = 1 \text{ cm}, T)$	$\epsilon_{\text{NFe}}(r_a = 10 \text{ cm}, T)$	$\epsilon_{\text{NairC}}(r_a = 1 \text{ cm}, T)$	$\epsilon_{\text{NairC}}(r_a = 10 \text{ cm}, T)$
e_8	1.93175025346655E+07	1.93175025346655E+07	-7.7215070428136E+06	1.4979755989820E+06
e_7	1.05744744269744E+07	1.05744744269744E+07	1.21673385504994E+07	-4.5275893600650E+06
e_6	1.76185683603940E+07	1.76185683603940E+08	7.12156143865781E+07	-9.4952021034798E+06
e_5	-2.82291919379242E+07	-2.82291919379242E+08	-6.09199599100066E+07	2.29875331739013E+07
e_4	-6.559402371252570E+08	-6.55940237125257E+08	-2.899492296329290E+08	1.31346032664877E+07
e_3	-2.86316893523397E+07	-2.86316893523397E+08	-1.02444324585236E+07	-3.04726895363733E+07
e_2	2.4682719876971300E+09	2.4682719876971300E+08	6.168294704590720E+08	1.058178447148170E+08
e_1	6.1142071770641700E+09	6.1142071770641700E+09	7.580636393041320E+08	2.511653301216220E+08
e_0	1.01625212197173000E+10	1.016252121971730E+09	3.224937271577620E+08	1.387875465974260E+08
e_m	1.42863323807 E+04	1.38837087603E+04	1.29782913165E+04	1.35589551213E+04
e_s	2.4905863447 E+03	2.5421012442E+03	3.3863339111 E+03	3.4380556550E+03

$\gamma = \frac{T-e_m}{e_s}, T$ in K

$\epsilon_{N_x}(r_a, T) = e_8 \gamma^8 + e_7 \gamma^7 + e_6 \gamma^6 + e_5 \gamma^5 + e_4 \gamma^4 + e_3 \gamma^3 + e_2 \gamma^2 + e_1 \gamma + e_0, \epsilon_{N_x}(r_a, T)$ in $\text{W sr}^{-1} \text{ m}^{-3}$

Annex B. Arc Length Formulas

In 1994, Bowman proposed the well-known formulas for the estimation of the radius and the voltage of a DC arc, as shown in Equation (35) and (36), respectively.^[7]

$$\frac{r_a(z)}{r_k} = 3.2 - 2.2e^{\left(-\frac{z}{5r_k}\right)} \quad (35)$$

$$V_a = \frac{2}{\sigma_o} \sqrt{\frac{I J_k}{\pi}} \frac{1}{r_k} \int_0^{l_a} \left(\frac{r_k}{r_a(z)}\right)^2 dz \quad (36)$$

Due to the complex mathematical nature of Equation (36), in industry, the length of the electric arc, both AC and DC, is traditionally estimated using a simplified empirical formula^[20,45]

$$l_a = \frac{V_a - V_{an-ac}}{E_a} \quad (37)$$

Equation (37) is derived from the assumption that the total arc voltage is the sum of the voltage drop in the cathode, anode, and column regions of the arc. The last was approximated as the multiplication of the electric field in the plasma column by its length.^[52] For the case of AC arcs, and neglecting any voltage drop at the high-current circuit of the EAF transformer (cables and electrodes), the RMS of the phase to neutral voltage (V_{RMS}) of the secondary side of the transformer is used as the arc voltage (V_a). For both AC and DC arcs, the literature reports that acceptable values for V_{an-ac} and E_a vary from 30 to 50 V and from 6 to 12 V cm⁻¹, respectively.^[20,45,52]

Acknowledgements

Financial support is gratefully acknowledged from the Marie Skłodowska Curie Horizon 2020 EID-ITN project—PROcess NeTwork Optimization for efficient and sustainable operation of Europe's process industries taking machinery condition and process performance into account (PRONTO), grant agreement no. 675215. The authors would like to thank Mauro Grifoni and Lucio Mancini for valuable discussions about the EAF operation and their support during the validation tests. The authors also acknowledge the production management team of Acciai Speciali Terni, Roberto Moretti, and Daniele Sguigna, for having allowed them to conduct the validation experiments of this study. Finally, the authors also thank the team of operators of the EAF for their cooperation during the experiments. Open access funding enabled and organized by Projekt DEAL.

Conflict of Interest

The authors declare no conflict of interest.

Keywords

electric arcs, Elenbaas–Heller equation, minimum entropy production, plasma, steelmaking

Received: July 15, 2020

Revised: September 22, 2020

Published online: October 21, 2020

- [1] J. Bakken, L. Gu, H. Larsen, V. Sevastyanenko, *J. Eng. Phys. Thermophys.* **1997**, *70*, 530.
- [2] G. Saevarsdottir, H. Loken, J. Bakken, in *8th Int. Ferroalloys Congress*, Beijing, China **1998**, pp. 317–322.
- [3] J. Sanchez, M. Ramirez-Argaez, A. Conejo, *Steel Res. Int.* **2009**, *80*, 113.
- [4] M. Sakulin, R. Hirtler, in *Simulationstechnik*, Springer, Berlin/New York **1984**, pp. 641–645.
- [5] A. Fathi, Y. Saboohi, I. Škrjanc, V. Logar, *ISIJ Int.* **2015**, *55*, 1353.
- [6] J. Gruber, H. Pfeifer, M. Kirschen, K. Krüger, *Development of a Numerical Model for the Heat and Mass Transport in an Electric Arc Furnace Freeboard*, RWTH-2016-01909, Lehrstuhl für Hochtemperaturtechnik und Institut für Industrieofenbau und Wärmetechnik **2016**.
- [7] B. Bowman, in *52nd Electric Furnace Conf.*, Nashville, USA **1994**, pp. 111–120.
- [8] H. Maecker, *The Electric Arc*, H Popp Matlab GmbH, Berg, Germany **2009**.
- [9] H. Kuiken, *Appl. Phys. Lett.* **1991**, *58*, 1833.
- [10] J. Lowke, *J. Appl. Phys.* **1970**, *41*, 2588.
- [11] J. Lowke, *J. Quant. Spectrosc. Radiat. Transf.* **1974**, *14*, 111.
- [12] G. Jordan, B. Bowman, D. Wakelam, *J. Phys. D: Appl. Phys.* **1970**, *3*, 1089.
- [13] B. Bowman, H. Edels, *J. Phys. D: Appl. Phys.* **1969**, *2*, 53.
- [14] P. Gueye, Y. Cressault, V. Rohani, L. Fulcheri, *J. Appl. Phys.* **2017**, *121*, 073302.
- [15] X. Zhou, J. Heberlein, *Plasma Sources Sci. Technol.* **1994**, *3*, 564.
- [16] H.-P. Li, E. Pfender, X. Chen, *J. Phys. D: Appl. Phys.* **2003**, *36*, 1084.
- [17] T. Christen, *Entropy* **2009**, *11*, 1042.
- [18] A. Di Vita, *Phys. Rev. E* **2010**, *81*, 041137.
- [19] R. G. Endres, *Sci. Rep.* **2017**, *7*, 1.
- [20] B. Bowman, K. Krüger, *Arc Furnace Physics*, Verlag Stahleisen GmbH, Düsseldorf, Germany **2009**.
- [21] A. Gleizes, J.-J. Gonzalez, P. Freton, *J. Phys. D: Appl. Phys.* **2005**, *38*, R153.
- [22] D. J. Griffiths, *Introduction to Electrodynamics*, Cambridge University Press, Cambridge, UK **2017**, p. 574.
- [23] J. Nilsson, S. Riedel, *Electric Circuits 9th*, Prentice Hall, New Jersey, USA **2011**.
- [24] T. Christen, *J. Phys. D: Appl. Phys.* **2006**, *39*, 4497.
- [25] A. Gleizes, Y. Cressault, P. Teulet, *Plasma Sources Sci. Technol.* **2010**, *19*, 055013.
- [26] M. Bartlova, V. Aubrecht, O. Coufal, *POBeo* **2010**, *89*, 241.
- [27] J. Menart, S. Malik, *J. Phys. D: Appl. Phys.* **2002**, *35*, 867.
- [28] J. Pousse, B. Chervy, J.-F. Bilodeau, A. Gleizes, *Plasma Chem. Plasma Process.* **1996**, *16*, 605.
- [29] Y. Wu, M. Li, M. Rong, F. Yang, A. Murphy, Y. Wu, D. Yuan, *J. Phys. D: Appl. Phys.* **2014**, *47*, 505204.
- [30] W. Zhen, W. Ninghui, L. Tie, C. Yong, *Plasma Sci. Technol.* **2012**, *14*, 321.
- [31] Steel Institute VDEh, in *Proc. 13th Int. Seminar VDEh on Electric Arc Furnaces*, Cologne, Germany **2017**.
- [32] Y. Goda, M. Iwata, K. Ikeda, S.-I. Tanaka, *IEEE Trans. Power Delivery* **2000**, *15*, 791.
- [33] Y. Lee, D. Gaskell, *Metall. Trans.* **1974**, *5*, 853.
- [34] F. R. Cheslak, J. A. Nicholls, M. Sichel, *J. Fluid Mech.* **1969**, *36*, 55.
- [35] H. Y. Hwang, G. A. Irons, *Metall. Mater. Trans. B* **2012**, *43*, 302.
- [36] H. Maecker, *Z. Phys.* **1955**, *141*, 198.
- [37] F. R. Cheslak, J. A. Nicholls, M. Sichel, *J. Fluid Mech.* **1969**, *36*, 55.
- [38] R. B. Banks, D. Chandrasekhara, *J. Fluid Mech.* **1963**, *15*, 13.
- [39] H. Y. Hwang, G. A. Irons, *Metall. Mater. Trans. B* **2012**, *43*, 302.
- [40] R. Jones, Q. Reynolds, T. Curr, D. Sager, *J. South. Afr. Inst. Min. Metall.* **2011**, *111*, 665.
- [41] M. Tawarmalani, N. V. Sahinidis, *Math. Program.* **2005**, *103*, 225.
- [42] N. V. Sahinidis, BARON 17.8.9: Global Optimization of Mixed-Integer Nonlinear Programs, User's Manual, <https://minlp.com/downloads/docs/baron%20manual.pdf> (accessed: October 2020).

- [43] F. Qian, B. Farouk, R. Mutharasan, *Metall. Mater. Trans. B* **1995**, 26, 1057.
- [44] J. Alexis, M. Ramirez, G. Trapaga, P. Jönsson, *ISIJ Int.* **2000**, 40, 1089.
- [45] R. Garcia-Segura, J. Vázquez Castillo, F. Martell-Chavez, O. Longoria-Gandara, J. Ortegón Aguilar, *Energies* **2017**, 10, 1424.
- [46] V. Logar, D. Dovžan, I. Škrjanc, *ISIJ Int.* **2012**, 52, 402.
- [47] R. D. MacRosty, C. L. Swartz, *Ind. Eng. Chem. Res.* **2005**, 44, 8067.
- [48] A. Fathi, Y. Saboohi, I. Škrjanc, V. Logar, *Steel Res. Int.* **2017**, 88, 1600083.
- [49] F. Opitz, P. Treffinger, J. Wöllenstein, *Metall. Mater. Trans. B* **2017**, 48, 3301.
- [50] T. Meier, K. Gandt, T. Hay, T. Echterhof, *Steel Res. Int.* **2018**, 89, 1700487.
- [51] J. D. Hernandez, L. Onof, S. Engell, in *Proc. of the 8th Int. Conf. on Modeling and Simulation of Metallurgical Processes in Steelmaking (STEELSIM 2019)*, Toronto, Canada **2019**, pp. 295–306.
- [52] A. Guile, in *Proc. of the Institution of Electrical Engineers*, Vol. 118, IET **1971**, pp. 1131–1154.